J Mater Sci (2022) 57:285–298

Chemical routes to materials

Residual stresses in the graded interlayer between W and CuCrZr alloy

Marcello Cabibbo[1], Alessandra Fava[2], Roberto Montanari[3], Ekaterina Pakhomova[4], Chiara Paoletti[1], Maria Richetta[3], and Alessandra Varone[3,*]

[1] *Dipartimento di Ingegneria Industriale e Scienze Matematiche, Università Politecnica delle Marche, Via Brecce Bianche 12, 60131 Ancona, Italy*
[2] *Dipartimento di Energia, Divisione di Ingegneria Nucleare, Politecnico di Milano, Piazza Leonardo da Vinci 32, 20133 Milan, Italy*
[3] *Dipartimento di Ingegneria Industriale, Università di Roma "Tor Vergata", Via del Politecnico 1, 00133 Rome, Italy*
[4] *Dipartimento di Ingegneria Meccanica, Chimica e dei Materiali, Università di Cagliari, Via Marengo 2, 09123 Cagliari, Italy*

Received: 10 September 2021
Accepted: 13 October 2021
Published online: 3 January 2022

ABSTRACT

One of the big challenges for realizing future nuclear fusion reactors is the development of materials able to withstand the high thermal loads and particle fluxes typical of these reactors. This work investigated the residual stresses in a W coating deposited through plasma spraying on a substrate of CuCrZr alloy used in the active cooling system of ITER (International Thermonuclear Experimental Reactor). To this purpose, a graded interlayer consisting of a mixture of W and Cu whose composition gradually changes was deposited between coating and substrate. The W coating-interlayer-CuCrZr substrate system showed good adhesion and no cracks were observed. Residual stresses were investigated by X-ray diffraction (XRD) and nanoindentation tests. Residual stresses in the interlayer have different sign in W (compressive) and in Cu (tensile) and reach their maximum value in the inner part of the interlayer where the relative amounts of the two deposited metals are similar. The main contribution to residual stresses comes from thermal stresses arising when deposited metal and substrate cool together from deposition temperature to ambient temperature owing to the different coefficients of thermal expansion (CTE). The residual stresses measured in W are always below the critical value for crack formation (275 ± 50 MPa) but not negligible. Based on present results, the optimization of deposition temperature seems to be the key for reducing residual stresses in the interlayer.

Handling Editor: Yaroslava Yingling.

Address correspondence to E-mail: alessandra.varone@uniroma2.it

https://doi.org/10.1007/s10853-021-06631-5

Introduction

In the last decades, relevant advancements have been made toward the realization of the international thermonuclear experimental reactor (ITER); however, many scientific and engineering issues remain to be solved. One of the big challenges is the choice of plasma-facing materials to protect structural components, divertor and cooling systems. These indeed need to withstand high thermal loads (5–20 MW m^{-2}) [1–4] and particle fluxes typical of nuclear fusion reactors; therefore, the main requirements are excellent thermo-mechanical properties, high melting point, high thermal conductivity, low physical sputtering, tritium retention and activation under neutron irradiation [5]. Owing to its properties, W is considered the most promising candidate for the armors protecting ITER divertor and DEMO first wall [6, 7]. A recent review paper of Linsmeier et al. [8] describes and discusses the key role played by W in the development of advanced high heat flux and plasma-facing materials, the involved problems and the proposed solutions.

Bulk W can be used to build up armors, but a significant drawback is represented by its bad machinability with consequent difficulty to manufacture parts of complex geometry, e.g., those to protect tubes, pipes or fittings of the cooling system. Recently, in order to overcome the problems related to the intrinsic W brittleness and the high ductile to brittle transition temperature (DBTT), the possibility of producing bulk W through spark plasma sintering (SPS) has been assessed [9, 10]. This process allows to get a well-controlled microstructure and improved mechanical properties. However, the aforementioned problems are not yet definitively solved.

An alternative solution consists in depositing W coatings on the components of cooling system made of a CuCrZr alloy (Elbrodur©) [7, 11]; however, the joining is a hard task for the great mismatch of coefficients of thermal expansion (CTE) of W and Cu alloys that leads to high residual stresses at the interface of two metals during cooling to ambient temperature. The arising stresses may induce the formation and propagation of cracks and the final detachment of coating from substrate either in the deposition process or during the operative life of the component. Moreover, during the deposition process the temperature of the substrate needs to be kept below $\sim$ 430 °C to avoid overaging of CuCrZr alloy and degradation of its mechanical properties.

A great deal of work has been made so far to identify suitable coating technologies, and the attention has been focused on plasma spray (PS) in vacuum or controlled atmosphere [12–14], physical vapor deposition (PVD) [15] and chemical vapor deposition (CVD) [16, 17]. In particular, PS appears to be highly attractive for its simplicity, low costs and the possibility to cover large surfaces. Some attempts have been also made to deposit W by means of atmospheric plasma spray (APS), but the coatings exhibit worse thermo-mechanical properties owing to the higher content of oxides and the residual porosity [18–21].

The feasibility of 5-mm-thick W coatings on CuCrZr substrates through PS in controlled atmosphere has been demonstrated by Riccardi et al. [12, 13], and the coatings have been proved to withstand heat fluxes up to 5 MW m^{-2} without significant detrimental effects on morphology, structure, integrity and mechanical properties [12, 22, 23]. This was made possible by the deposition of an interlayer between W and CuCrZr providing a soft interface with intermediate thermal expansion coefficient and better thermo-mechanical compatibility. The result represented a breakthrough; however, there was a critical issue, namely the chemical composition of the interlayer (thickness $\approx$ 800 μm). This consisted of a layer of pure Ni and a successive stratification of layers of grading mixtures of Al–12% Si and Ni–20% Al. Here, the presence of Ni is highly undesired in nuclear fusion applications since this element exhibits high activation under neutron irradiation and, also in low quantity, represents a serious concern for the operations and maintenance of the reactor.

On these grounds a different approach has been investigated. This consisted of an interlayer designed to be a functionally graded material obtained by depositing successive layers of Cu and W by gradually changing their reciprocal fractions. This way, the interlayer is made of the same elements of substrate and coating and no other element is present. The same method has been also used for depositing W on steels for structural applications in fusion reactors [24, 25].

Matějíček et al. [26] determined the residual stress profiles in mixed W–Cu layers through in situ coating properties (ICP) sensor [27] and found that they strongly depend on gradation profile and deposition parameters and increase under conditions resulting in stronger bonding between the splats.

The present work investigates the residual stresses in the interlayer through X-ray diffraction (XRD) and nanoindentation. Individually for each phase, XRD gives stress values averaged over a large area, while nanoindentation provides information on a local scale, i.e., inside the W and Cu splats of the interlayer. Since at least 20 years, nanoindentation technique is widely used to study the residual stresses and has been successfully applied to different materials [28–34].

Materials and methods

Sample preparation and characteristics

The deposition process of W on the CuCrZr (Cr 0.65, Zr 0.05, Cu balance wt%) substrate was carried out through the controlled atmosphere PS technique by using a mix of Ar–H_2 gases at a pressure of 600 mbar. After preliminary tests for optimizing the deposition conditions, the coating was prepared by using a torch-surface distance of 180 mm and a torch speed of 800 mm s^{-1}. The substrate temperature, measured by a thermocouple, was kept constant (180 ± 5 °C). The sample is a cylinder (diameter of 30 mm, height of 10.6 mm), the cross section of the sample is shown in Fig. 1a. The W powders consisted of particles with two different size: 15–35 μm and < 5 μm. The W coating is about 1.6 mm thick while the interlayer ~ 1.2 mm. The interlayer is a mixture of pure W and Cu whose composition gradually changes with the proportions for each deposition step reported in Table 1. In fact, the interlayer has been built up by depositing 8 layers with nearly the same thickness (150 μm) and different composition obtained by adjusting of the powder feed rates.

Observations of light microscopy (LM) and scanning electron microscopy (SEM) were carried out on the cross section. The micrographs at different magnification in Fig. 1b, c show the interlayer where W and Cu splats exhibit a complex and irregular morphology. The system W coating-interlayer-substrate shows good adhesion and no cracks were observed.

XRD measurements

To determine the residual stresses in CuCrZr substrate, Cu–W interlayer and W coating XRD measurements have been carried out in 7 different zones along the sample cross section by moving the sample with steps of 250 μm (see Fig. 2). XRD patterns have been collected in the 2Θ angular range 35–150° by using the Cu-Kα radiation (λ = 1.5408 Å) with 2Θ angular steps of 0.05° and counting time of 5 s per step. The zone illuminated by X-rays was a rectangular spot whose width changed with the 2Θ angle, while its length was constant (15 mm).

The relative intensities of XRD peaks have been used to evaluate possible textures in the examined zones.

To measure residual stresses, XRD precision peak profiles have been collected with 2Θ angular steps of 0.005° and counting time per step of 20 s. Residual stresses of Cu and W in the different zones have been determined by measuring the positions of Cu {220} and W {211} peaks, namely those at the highest angle with suitable intensity. In the conditions of present experiments, Cu {220} and W {211} peaks are in the 2Θ range 72–75° where the width of the X-ray spot was about 250 μm. Since the step of analysis and the width of X-ray spot had substantially the same value, the whole interlayer has been examined without zones of overlapping. In fact, the width of X-ray spot is larger than each deposition steps (150 μm); thus, each zone examined by XRD does not correspond to a single deposition step.

After background subtraction, the peak profiles have been fitted by Lorentzian curves to eliminate the $K\alpha_2$ component and determine the correct peak positions. The elastic strains have been calculated from the variation of interplanar spacings d with respect d_0, those of the stress-free material reported in the JCPDS-ICDD database (W-File 4-806, Cu-File 4-0836) [35]:

$$\varepsilon = \frac{d - d_0}{d_0} \tag{1}$$

For cubic structures, the relative error $\Delta d/d$ is given by [36]:

$$\frac{\Delta d}{d} = K \cos^2 \theta \tag{2}$$

being K a constant. The strains have been determined by the positions of Cu and W peaks at the highest angle with suitable intensity, and residual stresses have been then calculated through the equations of elasticity.

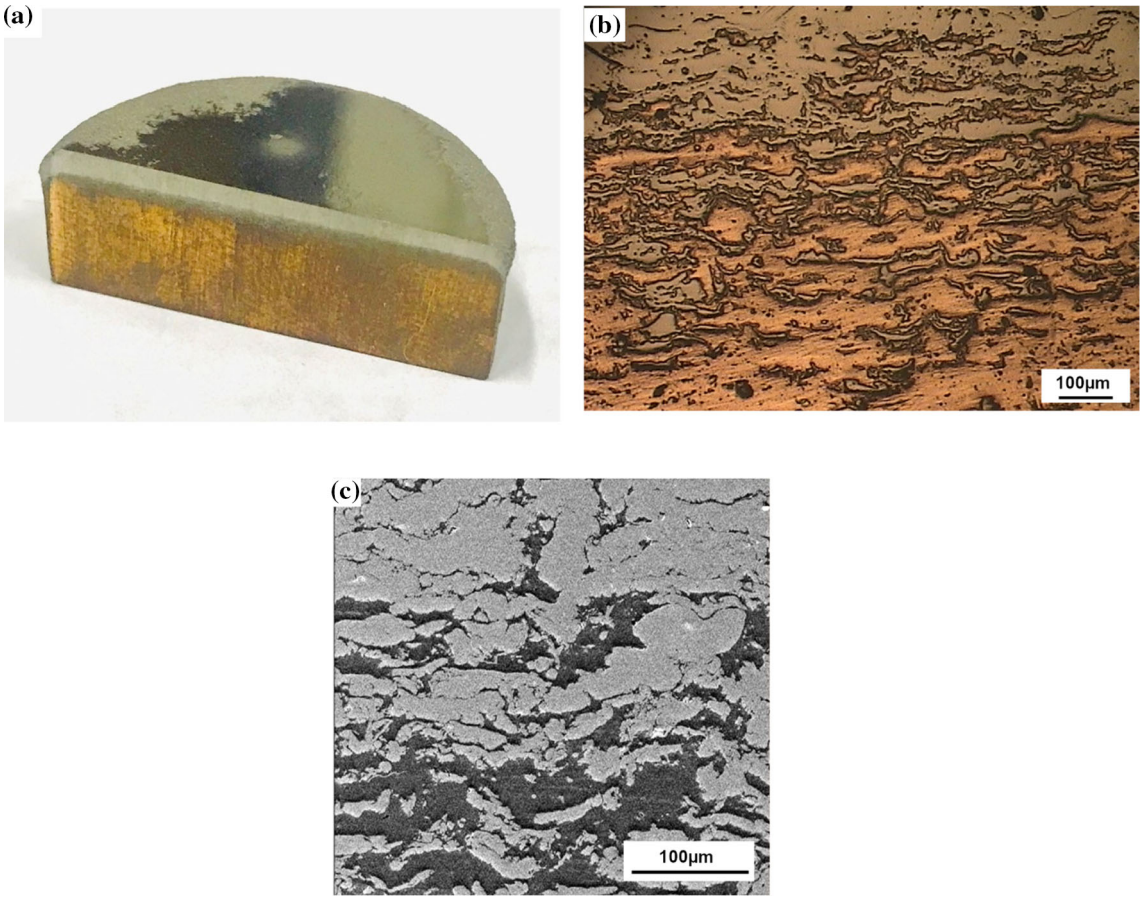

Figure 1 View of the sample (**a**), LM (**b**) and SEM (**c**) of Cu–W interlayer morphology.

Table 1 Deposition steps and interlayer composition for each step

Deposition steps	Interlayer composition	
	Cu vol.%	W vol.%
1	90	10
2	85	15
3	79	21
4	71	29
5	59	41
6	42	58
7	18	82
8	10	90
9	0	100

Nanoindentation tests

Reduced elastic modulus, E_r, and residual stresses have been measured by nanoindentation technique using a Hysitron© Inc. triboscope nanoindenter Ubi-1® (Minneapolis, MN, USA). Uniaxial compression has been performed using a 3-sided pyramidal Berkovich tip with edge aperture angle of 65.35° and tip curvature radius of 120 nm. The nanoindentation measurements have been analyzed using the Oliver and Pharr method [37–39]. Thence, E_r and residual stresses are determined by full cycles of load–unloading print. The unloading curve was fitted with the power-law relationship $P = B(h - h_f)^k$, where P is the tip load, h the displacement, h_f the displacement after unloading, B and k fitting parameters. The penetration contact depth, h_c, can be estimated by $h_c = h_{max} - \eta(P_{max}/S)$, where h_{max} is the maximum indenter penetration depth at the peak load, P_{max}, η is a tip-dependent constant that for a Berkovich tip is 0.75, and S the material stiffness. Calibration was carried out on fused quartz (E_r = 72 GPa) according to the specifications drawn by Cabibbo et al. [40]. With this regard, a trapezoidal load function, consisting of same load and unload rates at a speed of 5 s to the peak load P_{max} = 8 mN, and a dwelling peak load of 2 s, was used. In particular, in

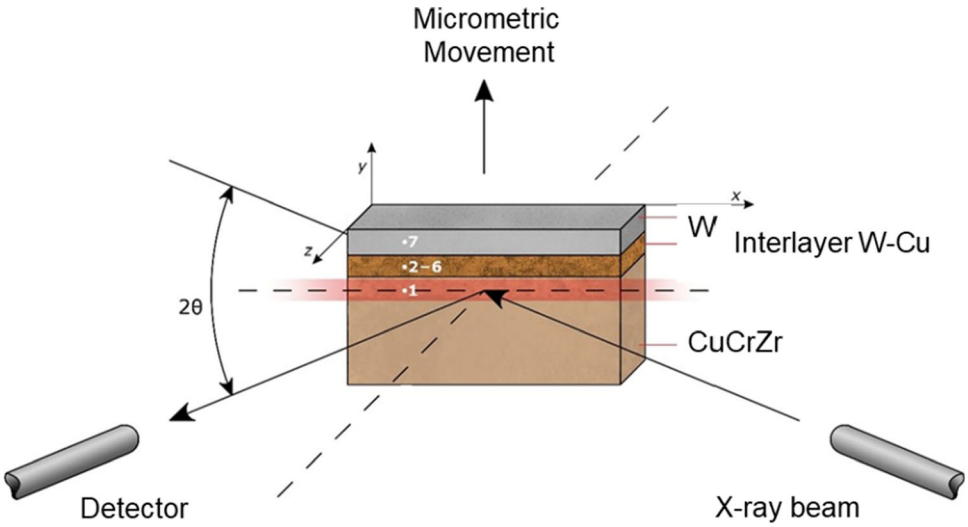

Figure 2 Schematic view of the experimental setup used in XRD measurements.

nanoindentation tests, load (P) and penetration depth (h) are measured step by step during a loading–unloading cycle. Figure 3 shows the effect of tensile and compressive stresses on the indentation curve. At a given penetration depth, h_t, with respect to P_B (load in the stress-free material), tensile and compressive stresses lead to lower and higher values, respectively [32, 34]. The differential indentation force $\sigma_H A$ induced by residual stresses is $P_C - P_B$ (compressive stress) or $P_A - P_B$ (tensile stress).

Young's modulus E has been obtained from the indentation curves. The reduced modulus E_r is calculated from the load–depth (P–h) curve and is described by the equation:

$$E_r = \frac{S}{2\gamma\beta\sqrt{A}}\sqrt{\pi} \tag{3}$$

being $S = dP/dh$ the stiffness, γ a correction factor varying according to indenter geometry, A the contact area at the maximum load P_{max}, β a shape factor depending on axisymmetric or symmetric indenters. The reduced modulus E_r is related to the Young's modulus by:

$$\frac{1}{E_r} = \left(\frac{1-\upsilon^2}{E} + \frac{1-\upsilon_I^2}{E_I}\right) \tag{4}$$

where υ_I and E_I are the Poisson's ratio and the Young's modulus of the indenter, respectively.

Nanoindentation measurements were spaced 50 μm apart and spanned from W to CuCrZr. Four different measurement runs were carried out to get a statistically sound series of data. In this respect, the obtained E_r and residual stress measurements at each characteristic zone, i.e., from CuCrZr substrate throughout the W full deposition zone, resulted from the average over four individual measurements carried out at a mean distance of 250 μm one to the other. Hence, a minimum of 80 measurements was carried out on full W deposition zones and CuCrZr alloy where no W traces were present, and a minimum of 16 measurements at each characteristic zone of the Cu–W interlayer was also carried out, that is at a 50-μm-wide pace, from CuCrZr substrate to full W deposition, according to Table 1.

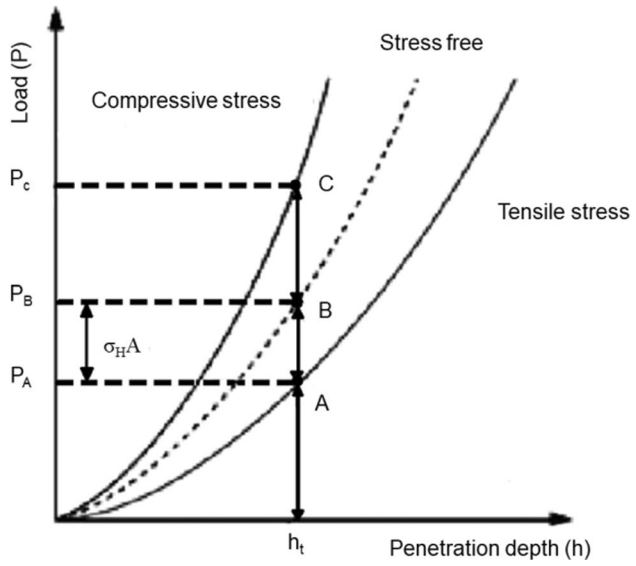

Figure 3 Effect of tensile and compressive state of stress on the load–depth (P–h) curve obtained by an indentation test.

Results

X-ray diffraction

The XRD patterns collected in the different zones across the interface are shown in Fig. 4. Only a part of the examined angular range is displayed because the peaks at higher angles were of negligible intensity and comparable to background.

Zone 1 is the CuCrZr substrate, while zone 7 is the W coating. The other zones correspond to successive shifts (250 μm) of the sample under the X-ray beam starting from the substrate and moving toward the W coating; in this way the whole interlayer has been examined.

By comparing the measured relative intensities with data taken from JCPDS X-ray database (W-4-806 and Cu-4-836 files) [35] referring to the metals with randomly oriented grains the preferred grain orientation have been estimated. This is important because nanoindentation can be affected by grain orientation [41].

The CuCrZr substrate (zone 1) has a strong <110> texture: The intensity of {220} peak is about 8 times that of Cu with randomly oriented grains. In addition to the principal <110> texture component, there is also the secondary <100> cubic one. In the first deposited layers (zones 2 and 3), these texture components become even stronger because the droplets of liquid Cu solidify with the same orientation of the grains forming the substrate. As the amount of W in the interlayer increases, this effect progressively weakens and Cu grains near the full W coating (zones 5 and 6) have an almost random orientation.

W in the zones 3 and 4 exhibits only a very weak {110} peak with intensity comparable to the background; thus, they are not suitable for describing a possible texture. In the zones 5, 6 and 7 the relative intensities do not strongly diverge from those corresponding to the random grain orientation.

Residual stresses of Cu and W in the different zones have been determined by measuring the positions of Cu {220} and W {211} peaks.

Figure 5a shows how the Cu {220} peak progressively shifts toward lower angles by passing from the substrate (zone 1) to zones 4–6 of the interlayer with increasing amount of W. The peak intensities have been normalized to favor the comparison.

The W {211} peak exhibits an opposite behavior: It shifts toward higher angles by passing from the coating of pure W (zone 7) to the zones 6–4 of the interlayer with increasing amount of Cu (Fig. 6). The W {211} peak position recorded in the coating of pure W corresponds to that of JCPDS-ICDD database (W-File 4-806); thus, it is substantially stress free. In fact, in a thin layer of W immediately close to the interlayer some stresses arise; however, they are small because W is deposited on a surface made of 90%W and 10%Cu. Successive W layers are deposited on a 100%W surface. The width of the X-ray spot is about 250 μm, and XRD gives a mean value of the examined area; thus, the peak position does not differ within the experimental error from that of JCPDS-ICDD database.

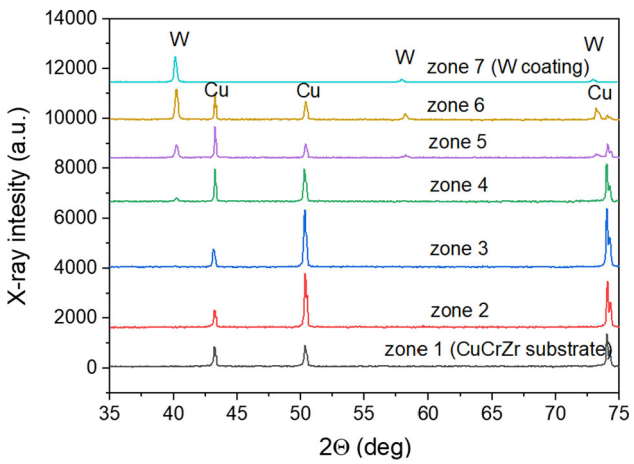

Figure 4 XRD patterns collected in the 7 different zones shown in Fig. 2.

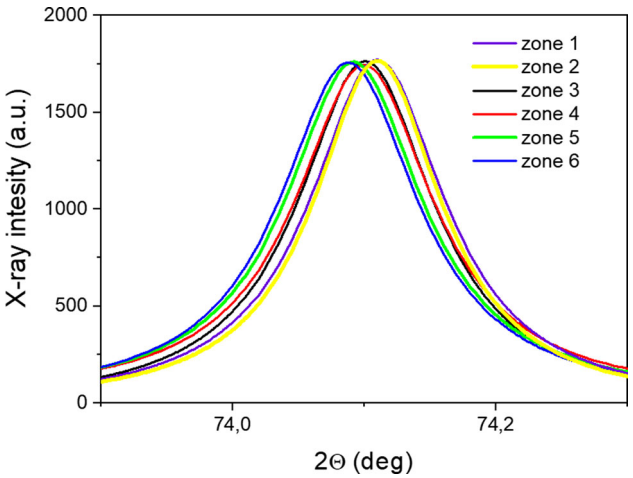

Figure 5 Progressive shift of the Cu {220} peak toward lower angles by passing from the substrate (zone 1) to the zones 4–6 of the interlayer with increasing amount of W.

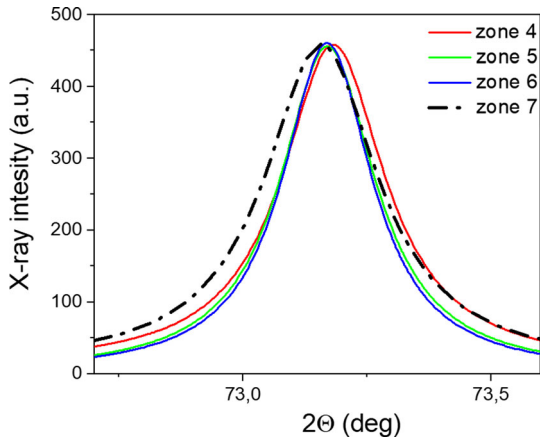

Figure 6 Progressive shift of the W {211} peak toward higher angles by passing from the coating (zone 7) to the zones 5–4 of the interlayer with increasing amount of Cu.

In the interlayer the shift of Cu {220} peak toward lower angles (Fig. 5) indicates that Cu is subjected to tensile strains along the z direction perpendicular to the examined surface, while W shows the opposite behavior (Fig. 6). Strains arise during solidification and cooling of the metal droplets after impacting on the substrate: The interface between W and Cu represents a constraint to the shrinkage of both the metals that have quite different thermal expansion coefficients α of Cu (16.6×10^{-6} °C^{-1}) and W (4.3×10^{-6} °C^{-1}). The constraint is in the plane (z–x) of PS deposition, while there are no constraints along the y direction of deposition; thus, $\sigma_y = 0$. Moreover, even if some differences on local scale may arise, it can be reasonably assumed that $\sigma_x = \sigma_z$ in the material volume involved in XRD analyses.

Thence, the strain along z direction has been determined out of the measured peak position shifts. The residual stresses ($\sigma_x = \sigma_z$) of Cu and W in the 7 different zones have been calculated from the following relationship:

$$\varepsilon_z = \frac{1}{E}\left[\sigma_z - \nu\left(\sigma_x + \sigma_y\right)\right] \quad (5)$$

being $\sigma_y = 0$, $E_W = 270 \pm 10$ GPa, $E_{Cu} = 86 \pm 3$ GPa and $\upsilon_W = 0.27$, $\upsilon_{Cu} = 0.34$ are the Young's modulus and Poisson's ratio of deposited W and Cu, respectively. Since Young's modulus of a PS-desposited metal is commonly different from that of the bulk one, the values of E_W and E_{Cu} used in the calculations have been determined by means of Eq. (4) from reduced moduli measured by nanoindentation tests. The results are reported in Table 2.

Nanoindentation

Nanoindentation has been used to determine the local elastic–plastic properties at a sub-micrometer scale. The interlayer region was then mechanically characterized by performing a series of indentation along line paths from CuCrZr substrate throughout the interlayer and down to the opposite W 100% deposition. At the interlayer, it resulted that, by the applied load of $P_{Max} = 8000$ μN, the indentation tip reached a penetration depth ranging 300–380 nm, in Cu. On the other hand, the penetration depth was halved (approximately 200 nm) in W. Using nanoindentation technique, the local reduced modulus, E_r, corresponding to the different chemical zones inside the interlayer was determined with an accuracy within 5%.

Figure 7 reports representative load–displacement nanoindentation curves recorded approximately at same interlayer locations as the ones from which XRD analyses were carried out. The two series of curves here reported refer to nanoindentation tests

Table 2 Strains ε and residual stresses ($\sigma_x = \sigma_z$) of Cu and W determined by XRD in the examined zones whose distance from substrate is reported inside brackets

Zone	Copper		Tungsten	
	ε	σ_x, σ_z (MPa)	ε	σ_x, σ_z (MPa)
1/CuCrZr substrate	2.3×10^{-4}	24 ± 6	–	–
2/(125 μm)	2.3×10^{-4}	24 ± 6	–	–
3/(375 μm)	3.4×10^{-4}	35 ± 7	–	–
4/(625 μm)	3.5×10^{-4}	36 ± 7	-2.9×10^{-4}	− 107 ± 21
5/(875 μm)	4.4×10^{-4}	45 ± 9	-3.0×10^{-4}	− 111 ± 22
6/(1125 μm)	4.6×10^{-4}	47 ± 9	-1.4×10^{-4}	− 52 ± 10
7/W coating	–	–		Stress free

The minus sign indicates compression stress, the plus sign tensile stress

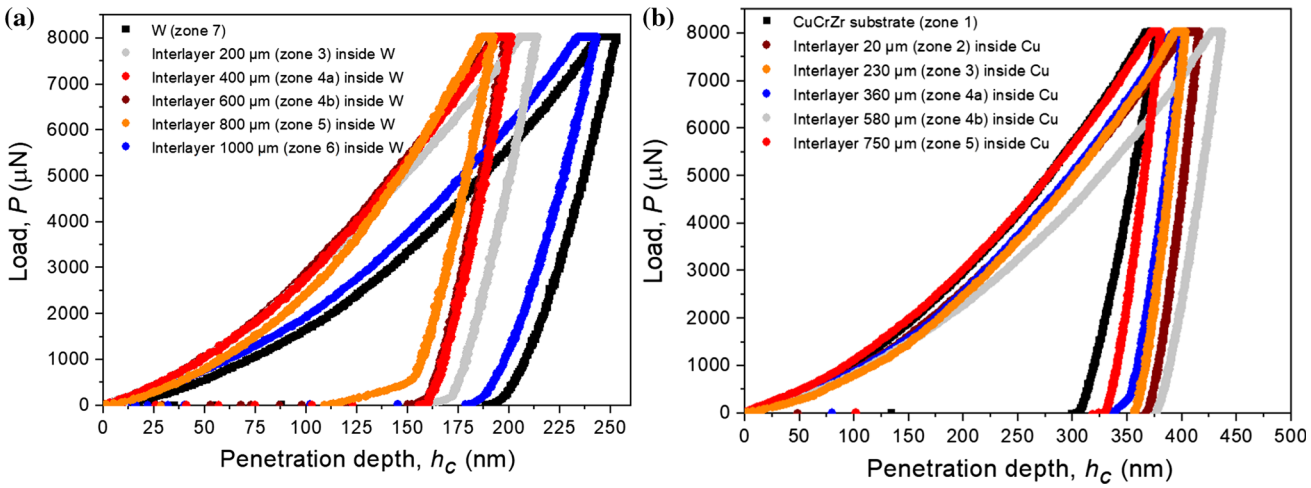

Figure 7 Representative load–displacement nanoindentation curves recorded within the interlayer. The curves reported in **a** refer to measurements taken inside W and are directly compared to a representative curve acquired in the 100% W coating region. The curves reported in **b** refer to measurements taken inside Cu and are compared to a representative curve acquired in the CuCrZr substrate.

Table 3 Values of residual stresses calculated from nanoindentation data by means of Eqs. (4)–(7)

	Zone	Residual stress σ (MPa)
Within W (compression)	2/(∼ 200 µm)	− 26 ± 2
	3/(∼ 400 µm)	− 76 ± 4
	4/(∼ 600 µm)	− 68 ± 4
	5/(∼ 800 µm)	− 115 ± 2
	6/(∼ 1000 µm)	− 22 ± 2
Within Cu (tensile)	2/(∼ 20 µm)	+ 14 ± 1
	2/(∼ 230 µm)	+ 14 ± 1
	3/(∼ 360 µm)	+ 11 ± 2
	4/(∼ 580 µm)	+ 23 ± 1
	5/(∼ 750 µm)	+ 7 ± 1

Nanoindentation tests in W and Cu were made in different zones of the interlayer whose distance from CuCrZr substrate is reported inside brackets. The sign minus indicates compression stress, the sign plus tensile stress

recorded at W (Fig. 7a) and Cu splats within the interlayer. From the evaluation and comparison of the nanoindentation curves reported in Fig. 7 the type (sign) and value of residual stresses in W and Cu have been determined (according to the schematic representation of Fig. 3).

The nanoindentation responses coming from W within the interlayer have been compared to that of the 100% W coating zone; those coming from Cu have been compared to that of the CuCrZr substrate.

It appeared that the loading section of the nanoindentation curves acquired inside W in the interlayer lies systematically on the left-hand side with respect to that in the W coating (Fig. 7a), indicating that the residual stresses are compressive. The opposite behavior is observed in the loading curves taken from Cu which are always on the right-hand side with respect to the reference curve taken in the CuCrZr substrate (Fig. 7b); thus, the stresses here are of tensile type.

The values of residual stresses referring to 5 different W and Cu areas at fixed distance from the CuCrZr substrate are reported in Table 3. Type and values of residual stresses here obtained by nanoindentation in W and Cu well agree with results obtained by XRD (Table 2). Recently, an analogous through-thickness stress distribution was observed in

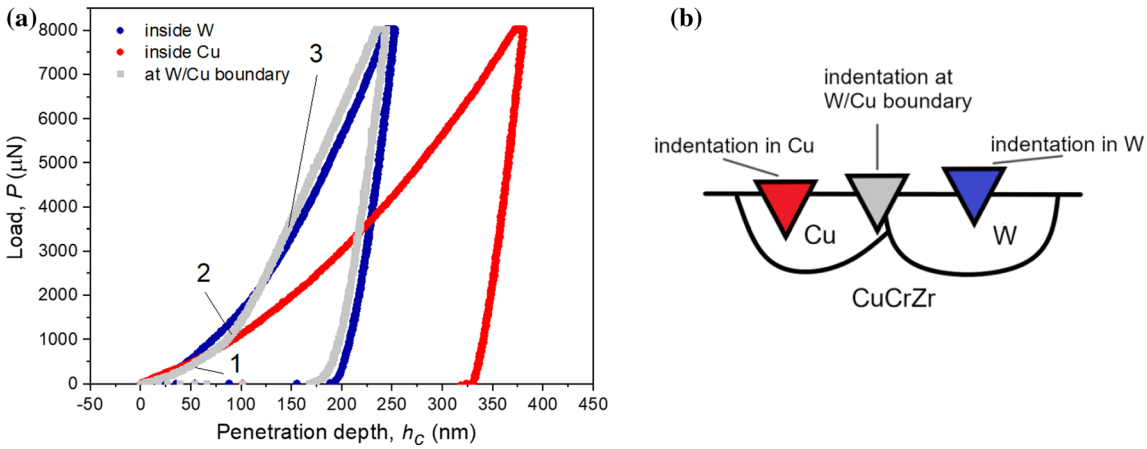

Figure 8 Representative load–displacement nanoindentation curves acquired in the Cu–W boundary (gray points), W (blue points) and Cu (red points) **a**; scheme view reproducing the nanoindentation positions, where colors correspond to the nanoindentation curves reported in **a**, **b**.

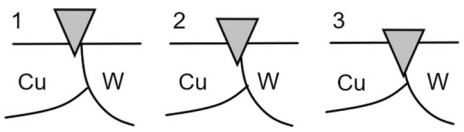

Figure 9 Three successive positions of the pyramidal Berkovich tip in a nanoindentation test made at the Cu–W boundary.

a 5-layer W–Cu coatings with graded composition [42].

A critical aspect of present tests was represented by nanoindentations taken at the boundary between W and Cu splats; the curves from these tests can introduce relevant errors in residual stress measures; thus, they had to be discarded. Direct microscopic inspection does not always guarantee a reliable identification of these occurrences; therefore, the curve shape has been used as a criterion to distinguish tests made in W or Cu splats from those in the boundary between splats of different metals.

To illustrate this issue and the followed procedure, a typical example of nanoindentation curves from tests carried out in three different positions (W, Cu and the boundary between them) is reported in Fig. 8a. A schematic view of indentations is displayed in Fig. 8b.

Figure 8b is just a sketch to illustrate how nanoindentation curves depend on the position of the indenter. The size of the indenter in the figure is exaggerated: W and Cu zones approximately range from 10 to 50 μm, and values much larger than the imprint (at the maximum penetration depth of ~ 500 nm the contact area is ~ 4 μm^2 and the imprint side ~ 3 μm).

To describe the mechanical response of the material when nanoindentation is taken at the Cu–W boundary (Fig. 8a) reference is made to Fig. 9 that shows three successive positions of the pyramidal Berkovich tip during the test. The parts 1, 2 and 3 of the gray curve in Fig. 8 a) substantially correspond to the successive positions of the indenter schematically shown in Fig. 9.

At the earlier loading stages, where the pyramidal tip touches and penetrates the Cu splat (Fig. 9-position 1), the load–displacement curve exhibits the typical response of Cu (red curve in Fig. 8a). In the reported example, this holds up to a loading $P \cong 800$ μN and a penetration depth, $h_c \cong 85$ nm. From this point on, the tip starts to interact also with the W splat (Fig. 9-position 2) and an abrupt slope change of the curve is observed (see gray-colored curve in Fig. 8a). Such interaction increases with indentation depth. Therefore, the curves acquired by testing Cu–W boundaries have been identified from the abrupt slope change that is not present in the curves obtained by indenting homogeneous areas (W or Cu). Moreover, since the volume contributing to the indentation response is significantly broader than the tip itself, a phase can interact with the indenting tip even if the tip is fully inside the other phase but sufficiently close to the interphase boundary. To eliminate this sort of 'mixed' indent events, the elastic modulus has been considered as an additional criterion of selection, namely the selection criterion was as

to take into account that of W or that of Cu, while curves with intermediate values have been discarded. A straightforward mean to distinguish the 'mixed' indentations was to carefully check and compare the loading indentation curves as to avoid a dual trend (loading penetration speed) that would come from a two-phase boundary zone. The gray-colored curve reported in Fig. 8 is a representative lading trend referring to a typical indentation on a boundary two-phase zone.

Discussion

As shown in Fig. 1b, the interlayer consists of W and Cu splats with irregular shape originated from the solidification of metal droplets impacting on the surface during the process of PS deposition.

Both XRD (Table 2) and nanoindentation (Table 3) evidenced that W in the interlayer exhibits residual compressive stresses, whereas in Cu there are tensile stresses. Since the cooling conditions change point by point also in a single layer, different splats of the same metal may exhibit different residual stresses. In fact, in addition to the effect of grain orientation, the scattering of nanoindentation data strongly depends on such local variability. Owing to the large size of the examined volume XRD provides values of residual stresses averaged on hundreds of W and Cu splats.

Residual stresses measured by nanoindentation are lower than those from XRD because the depth of analysis is few micrometers for nanoindentation and tens of micrometers for XRD. The examined cross section has been mechanically polished to remove surface irregularities because cutting residual stresses may be partially released in a very thin surface layer of few micrometers. Such unavoidable alteration affects much more nanoindentation than XRD and causes the observed difference. Anyhow, the most relevant result is that the stress trend provided by both techniques is substantially the same.

The origin of residual stresses in PS-deposited coatings is commonly believed to be due to two mechanisms. The first one refers to the constrained contraction of splats as they cool down in few milliseconds to the substrate temperature (quenching stresses σ_q); these stresses in splats are always tensile. The second one originates from the different contraction of deposited metal and substrate occurring as they cool together from deposition temperature to ambient temperature (thermal stresses σ_T). Thermal stresses may be compressive or tensile depending on the specific CTE values of metals of substrate and splat.

In fact, the net residual stress σ in W and Cu is the superposition of quenching and thermal stresses, namely $\sigma = \sigma_q + \sigma_T$.

Quenching stresses (first mechanism) can be expressed as [43, 44]:

$$\sigma_q = \alpha \Delta T E \tag{6}$$

where α is the CTE of deposited metal, E its Young's modulus and ΔT the temperature difference between molten metal and substrate. For the ΔT involved in the deposition process the σ_q values in W and Cu splats calculated by Eq. (6) are well above the yield stress of the metals; thus, plastic deformation occurs with consequent stress reduction. In fact, the extent of stress relaxation phenomena determines the effective quenching contribution to residual stresses. Similarly, thermal stresses (second mechanism) are affected by stress relaxation processes; however, relaxation is quite small because of the lower temperature and, in first approximation, it can be neglected.

Thermal stresses arise because CTE of Cu (16.6×10^{-6} °C^{-1}) is about 4 times that of W (4.3×10^{-6} °C^{-1}); thus, Cu undergoes a greater contraction than W during cooling from deposition temperature (T_D = 180 °C) to ambient temperature (T_0).

Figure 10 shows a schematic view of a Cu splat on a W layer. During cooling the contraction of Cu is constrained by the bond with W in the plane x–z, whereas is free in the y direction perpendicular to the

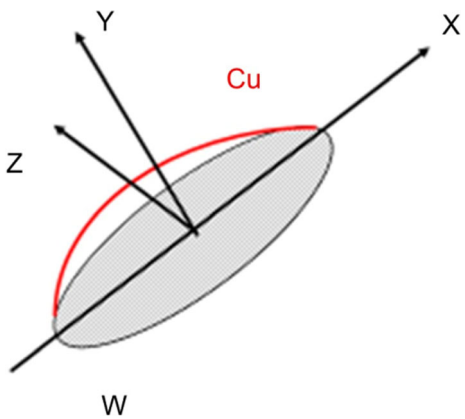

Figure 10 Schematic view of a Cu droplet solidified on W.

deposition surface. The constraint in the x–z plane leads to a reduced contraction of Cu; thus, tensile residual stresses arise in Cu, whereas the opposite effect takes place in W. The same phenomenon occurs if a W splat lies on Cu layer. On the contrary, in the case that the deposited metal is the same of substrate (W on W, or Cu on Cu) no stresses develop. On the average the thermal stresses in each metal are proportional to the probability that droplets fall on a zone of the other metal.

By assuming a perfect interface bonding between the two metals and that they exhibit an elastic behavior during cooling to ambient temperature, the thermal stress σ_T in a layer made of a single metal deposited on another one is given by [43]:

$$\sigma_T = (\alpha_D - \alpha_S)(T_D - T_0)E_D \quad (7)$$

where E_D is the Young's modulus at ambient temperature of deposited metal, α_D and α_S the CTE of deposited metal and substrate, respectively. However, in the case investigated here each layer is made of both metals; thus, to calculate σ_T the relative amounts of W and Cu, which gradually change along the interlayer, must be considered. For example, in the deposition of the nth layer the probability β that a Cu droplet falls on a W splat depends on the relative amount of Cu in the deposited layer (fraction of Cu droplets) and on the relative area covered by W in the $(n-1)$th layer. In order to simplify the calculation of the probability β, it has been assumed that all the droplets have the same volume and each splat on the surface has the shape of a parallelepiped. Under these conditions the relative area occupied by each metal in a deposited layer corresponds to its volume fraction in the sprayed powder; thus, β in the deposition of the nth layer can be written as:

$$\beta = f_n f_{n-1} \quad (8)$$

where f_n and f_{n-1} are the volume fractions of an element in the nth and $(n-1)$th layers, respectively. Based on the composition of the interlayer reported in Table 1, Eq. (8) has been used to calculate the probability β in each layer that W droplets fall on Cu and Cu droplets fall on W. The thermal stresses in each deposited layer can be now determined by:

$$\sigma_T = \beta(\alpha_D - \alpha_S)(T_D - T_0)E_D \quad (9)$$

The results are plotted in Fig. 11.

For both metals, thermal stresses reach their maximum value in the inner part of the interlayer where the relative amounts of the two metals are similar. Of course, the predictions inferred by using Eq. (9) represent only a rough estimation because physical phenomena involved in PS deposition are more complex than our assumptions. In particular, the model does not consider the possibility that a droplet falls on the boundary between W and Cu splats undergoing a not homogeneous cooling with a consequent stress gradient. Moreover, also the incipient melting of Cu substrate due to the impact of W droplets [45] is completely neglected. Anyway, the calculated trends (Fig. 11) substantially correspond to those of residual stresses measured by means of XRD and nanoindentation tests and absolute values are very close too. The difference between residual and thermal stresses should then be ascribed to quenching stresses. Residual stresses measured by XRD are a little higher than thermal stresses in the case of Cu, whereas the opposite is observed in W zones. For instance, for Cu the maximum σ_T is 30 MPa and 47 MPa is the value determined by XRD, whereas for W the values are 180 MPa and 111 MPa, respectively (Fig. 11).

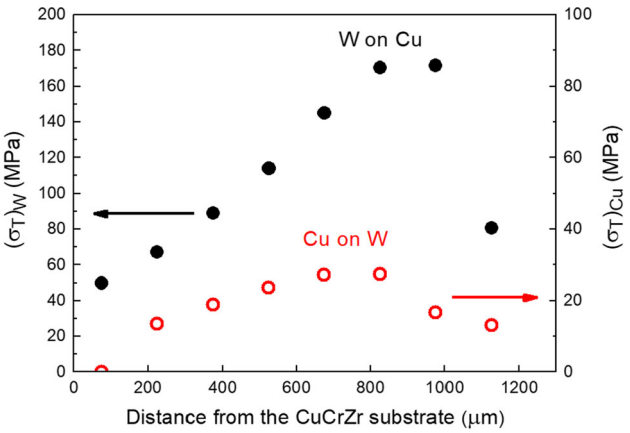

Figure 11 Absolute values of thermal stresses in W and Cu zones at increasing distance from the substrate. Stresses are of different sign (compressive in W, tensile in Cu). Data have been calculated by considering the interlayer composition reported in Table 1.

This result can be explained by considering that quenching stresses are always tensile and thus have the same sign of thermal stresses in Cu and opposite sign in W. Thence, they are added in the case of Cu and subtracted in the case of W.

Moreover, since the values of measured residual stresses and calculated thermal stress in both Cu and W are very close, present results suggest that large part of quenching stresses, even if not directly

measured, is accommodated by plastic deformation occurring in the deposited metals during the abrupt cooling to deposition temperature.

Investigations by Ganne et al. [46] on fracture behavior of deposited W assessed that, independently on the coating thickness, there is a critical stress for crack formation of 275 ± 50 MPa. Such value is in good agreement with previous results of Harry et al. [47]. Therefore, the residual stresses of W revealed by present experiments in the examined zones of the interlayer are well below the critical value but not negligible; thus, in presence of an external applied load, they can give a significant contribution to reach the critical stress for crack nucleation. Moreover, it is worthy to remind that W armors will be subjected to high flux plasma under cyclic heat loads; under these conditions the permeation of hydrogen isotopes gives rise to hydrogen bubbles of nanometric size which bring an extra hardening and prevent the release of the thermomechanical stresses [48]. On these grounds, deposition process should be improved for further reducing the residual stresses in the interlayer. Present results indicate that the substrate temperature during deposition is the principal parameter affecting thermal stresses which represent the main contribution to residual stresses. Therefore, the optimization of deposition temperature appears to be the key parameter for stress reduction.

Conclusions

This work investigated the residual stresses of a W coating deposited through PS in Ar-H_2 atmosphere on a substrate of CuCrZr focusing the attention on the interlayer with gradually changing fractions of Cu and W. The results can be summarized as follows.

1. The system W coating-interlayer-CuCrZr substrate shows good adhesion, and no cracks have been observed.
2. The interlayer consists of W and Cu splats which exhibit a complex and irregular morphology. XRD revealed that W and Cu exhibit a preferred grain orientation variation with the position across the interlayer.
3. Residual stresses in the interlayer have different signs: compressive in W and tensile in Cu. They reach the maximum value in the inner part (mid-width) of the interlayer where the relative amounts of the two deposited metals are similar.
4. The values of residual stresses measured by XRD and nanoindentation tests are close to those of thermal stresses; therefore, large part of quenching stresses seem to be accommodated by yielding.
5. Residual stresses measured in W inside the interlayer are well below the critical value for crack formation (275 ± 50 MPa [46]), although not negligible. Thence, under external applied load, these could contribute to reach the critical stress level.
6. On the basis of the reported results, the deposition temperature appears to be the key parameter for reducing residual stresses in the Cu–W interlayer.

Declarations

Conflict of interest The authors declare that they have no conflict of interest.

References

[1] Linke JM, Hirai T, Rödig M, Singheiser LA (2017) Performance of plasma-facing materials under intense thermal loads in tokamaks and stellarators. Fusion Sci Technol 46:142–151

[2] Linsmeier Ch, Unterberg B, Coenen JW, Doerner RP, Greuner H, Kreter A, Linke J, Maier H (2017) Material testing facilities and programs for plasma facing component testing. Nucl Fusion 57:092012

[3] Ueda Y, Schmid K, Balden M, Coenen JW, Loewenhoff Th, Ito A, Hasegawa A, Hardie C, Porton M, Gilbert M (2017) Baseline high heat flux and plasma facing materials for fusion. Nucl Fusion 57:092006

[4] Merola M, Escourbiac F, Raffray R, Chappuis P, Hirai T, Martin A (2014) Overview and status of ITER internal components. Fusion Eng Des 89:890–895

[5] Linke J, Du J, Loewenhoff Th, Pintsuk G, Spilker B, Steudel I, Wirtz M (2019) Challenges for plasma-facing components in nuclear fusion. Matter Radiat Extremes 4:056201

[6] Hirai T, Panayotis S, Barabash V, Amzallag C, Escourbiac F, Durocher A et al (2016) Use of tungsten material for the ITER divertor. Nucl Mater Energy 9:616–622

[7] You JH, Visca E, Bachmann C, Barrett T, Crescenzi F, Fursdon M et al (2016) European DEMO divertor target:

operational requirements and material-design interface. Nucl Mater Energy 9:171–175

[8] Linsmeier Ch, Rieth M, Aktaa J, Chikada T, Hoffmann A, Hoffmann J et al (2017) Development of advanced high heat flux and plasma-facing materials. Nucl Fusion 57:092007

[9] Terentyev D, Vilémová M, Yin C, Veverka J, Dubinko A, Matějíček J (2020) Assessment of mechanical properties of SPS-produced tungsten including effect of neutron irradiation. Int J Refract Hard M 89:105207

[10] Matějíček J, Veverka J, Yin C, Vilémová M, Terentyev D, Wirtz M, Gago M, Dubinko A, Hadraba H (2020) Spark plasma sintered tungsten—mechanical properties, irradiation effects and thermal shock performance. J Nucl Mater 542:152518

[11] Lipa M, Durocher A, Tivey R, Huber T, Schedler B, Weigert J (2005) The use of copper alloy CuCrZr as a structural material for actively cooled plasma facing and in vessel components. Fusion Eng Des 75–79:469–473

[12] Riccardi B, Pizzuto A, Orsini A, Libera S, Visca E, Bertamini L et al (1998) Tungsten thick coatings for plasma facing components. Fusion Technol 31:223–226

[13] Riccardi B, Montanari R, Casadei M, Costanza G, Filacchioni G, Moriani A (2006) Optimisation and characterisation of tungsten thick coatings on copper based alloy substrates. J Nucl Mater 352:29–35

[14] Vaßen R, Rauwald KH, Guillona O, Aktaa J, Weber T, Back HC, Qu D, Gibmeier J (2018) Vacuum plasma spraying of functionally graded tungsten/EUROFER97 coatings for fusion applications. Fusion Eng Des 133:148–156

[15] Bang E, Choi H, Kim HC, Kim K, Hong SH (2019) Manufacturing and testing of flat type W/Cu/CuCrZr mock-ups by HIP process with PVD coating. Fusion Eng Des 146:603–608

[16] Lian Y, Liu X, Wang J, Feng F, Lv Y, Song J, Chen J (2016) Influence of surface morphology and microstructure on performance of CVD tungsten coating under fusion transient thermal loads. Appl Surf Sci 390:167–174

[17] Lian Y, Feng F, Wang J, Liu X, Song J, Wang Y, Chen Z, Chen J (2019) Effect of high temperature annealing on the microstructure and thermal shock resistance of tungsten coatings grown by chemical vapor deposition. J Nucl Mater 513:241–250

[18] Heuer S, Matějíček J, Vilémová M, Koller M, Illkova K, Veverka J et al (2019) Atmospheric plasma spraying of functionally graded steel/tungsten layers for the first wall of future fusion reactors. Surf Coat Technol 366:170–178

[19] Huang JJ, Li XJ, Chen J, Liu Y, Qi B, Jiang SS, Wang X, Luo G (2013) Vacuum annealing enhances the properties of a tungsten coating deposited on copper by atmospheric plasma spray. J Nucl Mater 432:16–19

[20] Park JY, Yang SJ, Jin YG, Chong RP, Kim GH, Han HN (2014) Effect of annealing with pressure on tungsten film properties fabricated by atmospheric plasma spray. Met Mater Int 20:1037–1042

[21] Wang F, Luo GN, Huang J, Liu Y (2019) Properties improvement of atmospheric plasma sprayed tungsten coating by annealing. Surf Coat Technol 358:276–281

[22] Riccardi B, Montanari R, Moreschi LF, Sili A, Storai S (2001) Mechanical characterization of fusion materials by indentation test. Fusion Eng Des 58–59:755–759

[23] Montanari R, Riccardi B, Volterri R, Bertamini L (2002) Characterisation of plasma sprayed W coatings on a CuCrZr alloy for nuclear fusion reactor applications. Mater Lett 52:100–105

[24] Emmerich T, Qu D, Vaßen R, Aktaa J (2018) Development of W-coating with functionally graded W/EUROFER-layers for protection of First-Wall materials. Fusion Eng Des 128:58–67

[25] Heuer S, Li BS, Armstrong DEJ, Zayachuk Y, Linsmeier Ch (2020) Microstructural and micromechanical assessment of aged ultra-fast sintered functionally graded iron/tungsten composites. Mater Des 191:108652

[26] Matějíček J, Chraska P, Linke J (2007) Thermal spray coatings for fusion applications—review. J Therm Spray Technol 16:64–83

[27] Matějíček J, Sampath S (2003) In situ measurement of residual stresses and elastic moduli in thermal sprayed coatings part 1: apparatus and analysis. Acta Mater 51:863–872

[28] Zhao M, Chen X, Yan J, Karlsson AM (2006) Determination of uniaxial residual stress and mechanical properties by instrumented indentation. Acta Mater 54:2823–2832

[29] Jang JI (2009) Estimation of residual stress by instrumented indentation: a review. J Ceram Process Res 10:391–400

[30] Bocciarelli M, Maier G (2007) Indentation and imprint mapping method for identification of residual stresses. Comput Mater Sci 39:381–392

[31] Zhu L, Xu BS, Wang HD, Wang CB (2010) Measurement of residual stress in quenched 1045 steel by the nanoindentation method. Mater Charact 61:1359–1362

[32] Chen X, Yan J, Karlsson AM (2006) On the determination of residual stress and mechanical properties by indentation. Mater Sci Eng A 416:139–149

[33] Carlsson S, Larsson PL (2001) On the determination of residual stress and strain fields by sharp indentation testing. Part I: theoretical and numerical analysis. Acta Mater 49:2179–2191

[34] Carlsson S, Larsson PL (2001) On the determination of residual stress and strain fields by sharp indentation testing

Part II: experimental investigation. Acta Mater 49:2193–2203
[35] JCPDS-International Centre for Diffraction Data, Newtown Square.
[36] Cullity BD (1977) Elements of x-ray diffraction, 2nd edn. Addison-Wesley Publishing Company INC, Reading
[37] Pharr GM, Oliver WC, Brotzen FR (1992) On the generality of the relationship among contact stiffness, contact area, and elastic modulus during indentation. J Mater Res 7:613–617
[38] Oliver WC, Pharr GM (1992) An improved technique for determining hardness and elastic modulus using load and displacement sensing indentation experiments. J Mater Res 7:1564–1583
[39] Pharr GM (1998) Measurement of mechanical properties by ultra-low load indentation. Mater Sci Eng A 253:151–159
[40] Cabibbo M, Ricci P, Cecchini R, Rymuza Z, Sullivan J, Dub S, Cohen S (2012) An international round-robin calibration protocol for nanoindentation measurements. Micron 43:215–222
[41] Yua H, Das S, Yu H, Karamched P, Tarleton E, Hofmann F (2020) Orientation dependence of the nano-indentation behaviour of pure Tungsten. Scr Mater 189:135–139
[42] Matějíček J, Mušálek R, Veverka J (2019) Materials and processing factors influencing stress evolution and mechanical properties of plasma sprayed coatings. Surf Coat Technol 371:3–13
[43] Kuroda S, Clyne TW (1991) The quenching stress in thermally sprayed coatings. Thin Solid Films 200:49–66
[44] Tsui YC, Clyne TW (1997) An analytical model for predicting residual stresses in progressively deposited coatings. Part 1: planar geometry. Thin Solid Films 306:23–33
[45] Dallaire S (1982) Influence of temperature on the bonding mechanism of plasma-sprayed coatings. Thin Solid Films 95:237–244
[46] Ganne T, Crepin J, Serror S, Zaoui A (2002) Cracking behaviour of PVD tungsten coatings deposited on steel substrates. Acta Mater 50:4149–4163
[47] Harry E, Rouzaud A, Ignat M, Juliet P (1998) Mechanical properties of W and W(C) thin films: Young's modulus, fracture toughness and adhesion. Thin Solid Films 332:195–201
[48] Terentyev D, Dubinko V, Bakaev A, Zayachuk Y, Van Renterghem W, Grigorev P (2014) Dislocations mediate hydrogen retention in tungsten. Nucl Fusion 54:042004